



# Complex sliding characteristics of landslides and evaluation of the reinforcement with arched anti-slide piles based on 3D discrete element method: a case study

Qiang Xie<sup>1</sup> · Zhilin Cao<sup>1</sup> · Renjun Tian<sup>1,2</sup> · Weichen Sun<sup>1</sup> · Alessio Fumagalli<sup>3</sup> · Haiyou Peng<sup>1,4,5</sup> · Xiang Fu<sup>6</sup> · Haoyang Luo<sup>1</sup>

Received: 25 August 2023 / Accepted: 14 March 2024  
© The Author(s), under exclusive licence to Springer Nature B.V. 2024

## Abstract

Landslide movement processes often exhibit complex paths, introducing the uncertainty of landslide movement paths, and challenging landslide hazard prediction and pre-disaster prevention and control. In this study, we employed numerical simulations to investigate the dynamic processes with complex paths of the Pangjiawan landslide using the 3D discrete element method. A scenario simulation was conducted to evaluate the stability of the landslide, incorporating arched anti-slide piles, and the reinforcing effect of arch anti-slide piles on the Pangjiawan landslide under different rise-span ratios and pile spacing was analyzed in depth. The results indicate that the Pangjiawan landslide in mountainous notch topography exhibits a complex movement path with turning and convergence behaviors, and arched anti-slide piles are more effective in stabilizing the landslide than traditional linear anti-slide piles. When the embedded depth of the arched anti-slide piles remains consistent, higher rise-span ratios result in more significant synergistic effects between the piles and the surrounding soil. Moreover, even with increased pile spacing and a reduction in the number of anti-slide piles, the landslide displacement after reinforcement with arched anti-slide piles is lower than traditional linear anti-slide piles. The research provides valuable insights into the dynamics of landslide movements, emphasizing the superior reinforcement capabilities of arched anti-slide piles. This contributes to our understanding of landslide mitigation strategies in challenging topography.

**Keywords** Pangjiawan landslide · Mountain-notch topography · Complex moving path · Arched anti-slide piles · Discrete element method

## 1 Introduction

Landslides are widely distributed serious geological disasters, often causing casualties, economic losses, and even catastrophic consequences (Zhu et al. 2022; Fan et al. 2021; Froude and Petley 2018; Lu et al. 2014; Xu et al. 2014). A landslide is a natural sliding process due to many factors (Zhang et al. 2022a, b; Tian et al. 2021; Wang et al. 2020; Evans et al. 2001), such as earthquakes, rainfall, internal unstable structure, etc. Of these,

---

Extended author information available on the last page of the article

landslide hazards induced by rainfall-induced reduction in rock mass strength are the most prevalent (Hu et al. 2022; Zhang et al. 2022a, b; Lu et al. 2014). After the start of a landslide, its sliding characteristics combines a variety of complex movement path disturbed by the topography of the natural sliding path. The complex movement path of a natural landslide is significantly different from the ideal path of a simple slider, leaning against a heavy force moving down a flat slope (Kumar and Chandrasekaran 2022; Gao et al. 2017; Huang et al. 2019; Li et al. 2020; Schaefer et al. 2021; Yin et al. 2016). Some scholars (Bessette-Kirton et al. 2020; Schaefer et al. 2021; Li and Lan 2021) have summarised six prevalent and essential complex behaviors of landslide movement paths: spreading, turning, splitting, braiding, coalescence, and connection. Studying the sliding process of a landslide can help us to understand the characteristics of landslide movement paths, which offer the further understanding to evaluate the risk of landslides, prevent and control them, and reduce the threat to the economy and the natural environment.

Numerical simulation is currently one of the most effective means to study the sliding characteristics of large-scale landslides (Wu et al. 2022). Compared with continuum element methods, the discrete element method (DEM) provides the assumption of discontinuity in the soil-rock medium (Cundall and Strack 1979). It has the advantages of simulating large engineering deformation and visually analyzing the sliding characteristics of landslides (Cundall and Strack 1979). Discontinuous deformation analysis (DDA) (Chen and Wu 2018; Huang et al. 2019), block discrete element method (3DEC, UDEC) (Wu et al. 2017, 2018), matrix computing of discrete element method (MatDEM) (Gianvito et al. 2018; Li et al. 2022), and particle flow code (PFC2D/3D) (Li et al. 2021; Lin and Lin 2015; Ray et al. 2022; Shi et al. 2016; Zhuang et al. 2022) are all applied to simulate the landslide dynamic sliding process. For studies of the complex motion process of landslides, due to the advantage of more accuracy in solving large deformations of granular materials, PFC2D/3D is widely used to simulate the landslide process (Wang et al. 2020). Through PFC2D/3D, Lo et al. (2011) investigated a landslide movement process and accumulation scope, and the results showed that the discrete element method is an effective method to assess the severity of landslide damage with complex deformation. Lu et al. (2014) simulated the damage process of a landslide where dispersion motion paths occurred under heavy rainfall conditions and used the information on landslide movement paths, particle velocities, and landslide-affected areas to contribute to landslide hazard assessments. Wei et al. (2019) established a numerical model of the Mabian landslide and analyzed its movement paths in terms of velocity, displacement, energy, etc. Meng et al. (2022) simulated the process of Sanyang landslide movement, and the results showed that the direction of this landslide movement was deflected twice, from  $60^\circ$  to  $115^\circ$  (obstructed by the mountain) and from  $115^\circ$  to  $50^\circ$  (under the influence of the terrain). The above investigations provide meaningful insights into landslide sliding under complex paths in different topography.

Anti-slide piles are among the most common remedial measures in landslide reinforcement engineering (Usluogullari et al. 2016; Xie et al. 2021a, 2021b). For different geological conditions, landslide scale, and project requirements, different types of anti-slide piles have been developed, such as the liner cantilever anti-slide pile (Hu et al. 2017), the anchored anti-slide pile (Zhang et al. 2021), the double-row anti-slide pile (the combined pile (Kim et al. 2012)) and the h form type anti-slide pile (Zhao et al. 2017), and others. When a landslide occurs in notched topography, such as a V-shaped, gully area. The bedrock on both sides of the sliding body has greater thickness and better structural stability compared to the bedrock in the lower part of the sliding body, so arched anti-piles that further utilize the bedrock on both sides of the sliding body to carry the load are proposed (Xu 2012; Zhang and Deng 2013). The landslide in mountain-notch topography usually has the

characteristics of complex movement paths with multiple behaviors, which are influenced by the inclination and tendency of the notch topography. However, there are few studies on the effect evaluation of the reinforcement of arched anti-slide piles to landslides with mountain-notch topography under complex movement paths, especially the stability analysis of arched anti-slide piles with different design parameters, which seriously restrict the application of arched anti-slide piles in mountain-notch topography.

The purpose of this paper is to analyze the complex sliding characteristics of the Pengjiawan landslide and to evaluate the reinforcement effectiveness of arched anti-slide piles on this landslide under different design parameters. First, a field investigation was carried out to interpret the characteristics and failure mechanism of the Pangjiawan landslide. Second, the PFC3D was applied to simulate large-scale deformation, including initial failure, multiple behaviors within the movement, and the eventual deposition. Finally, we discuss the scenario simulation of the arched anti-slide pile to reinforce Pangjiawan landslides, focusing on the influence of different rise-span ratios and pile spacing.

## 2 Characteristics of the Pangjiawan landslide

### 2.1 Overview of the Pangjiawan landslide

The Pangjiawan landslide was induced by the long-term heavy rainfall that occurred in July 2020 in Chengkou County, Chongqing City, Southwest China. The landslide occurred on the right bank of the Pingba River (Fig. 1). The geographic coordinates of the landslide are  $108.494^{\circ}$ – $108.498^{\circ}$  East and  $32.0067^{\circ}$ – $32.0089^{\circ}$  North. According to the observation data of Chengkou County Meteorological Bureau, Chengkou is located in the Dabashan rainstorm area, one of Sichuan's four major rainstorm areas. The area receives abundant rainfall throughout the year, with an average annual precipitation day of  $\geq 0.1$  mm of 166 days. The area has high mountains and deep valleys, large differences in topographic elevation, and is characterized by a mountainous, three-dimensional climate.



Fig. 1 Remote-sensing image of the study area

The terrain slope angle of the Pangjiawan landslide is 10–20°. The slope aspect of the upper part of the landslide is 63°, and the slope aspect of the lower part is 104°. The longitudinal length of the landslide is approximately 110 m, the horizontal width is 70 m, the area is 0.77e4 m<sup>2</sup>, the average thickness is 11.83 m, and the volume is about 9.10e4 m<sup>3</sup>. The visible deformation of the landslide during the survey was mainly ground cracking, with a length of 30–50 m and width of 0.03–0.30 m, at the back edge of the landslide, and localized soil slides at a distance of 0.5–12 m at the front edge of the landslide as shown in Fig. 2. Because of the topography's undulation on the landslide's western side, the main direction of movement was deflected from 63° to 104°.

## 2.2 Engineering hydro-geological characteristics

The Pangjiawan landslide elevation surface is shown in Fig. 3. The Pangjiawan landslide is generally high in the west and low in the east, with a highest elevation of 638 m and lowest elevation of 598 m. Figure 4 shows geological sections I-I and II-II of the Pangjiawan landslide and the distribution of sections is shown in Fig. 2. Based on field investigations and geological surveys, the landslide source area (sliding body) was found to be mainly earthy yellow clay, with a small number of gravel particles. Bedrock is mainly limestone. In the soil-rock contact zone, the gravel particles are generally 10–25 mm in diameter, and comprise strongly weathered, sub-angular to sub-rounded fragments with no directional arrangement, and no contact between the gravel particles; there are voids between the gravel particles, as shown in Fig. 4a.

The groundwater level in the landslide area is deeply buried. The source area of the landslide is only affected by the upper layer of stagnant water, which is mainly distributed in the clay, recharged by atmospheric precipitation, with the characteristics of nearby recharge and discharge, short runoff distance, and easy discharge. The sliding bed is mainly limestone, which belongs to the relatively watertight layer, and the surface water, after percolating along the clay to the soil-rock interface, will be discharged downward along the rock-soil interface.

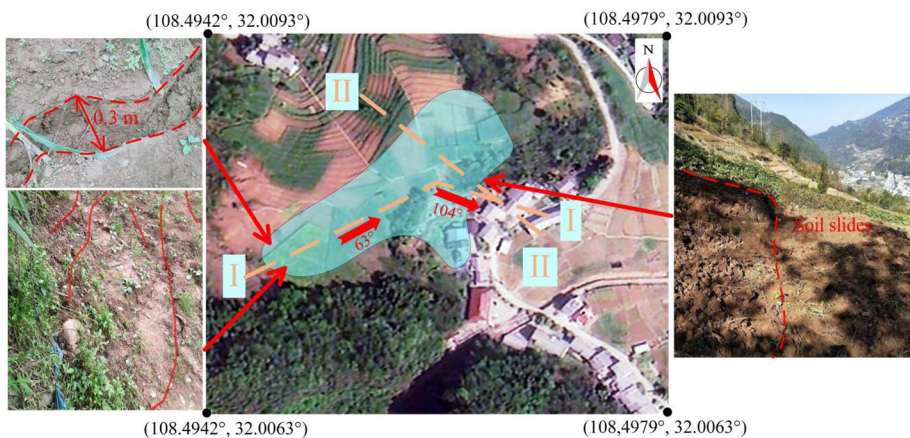


**Fig. 2** Plane form of landslide and field measurements

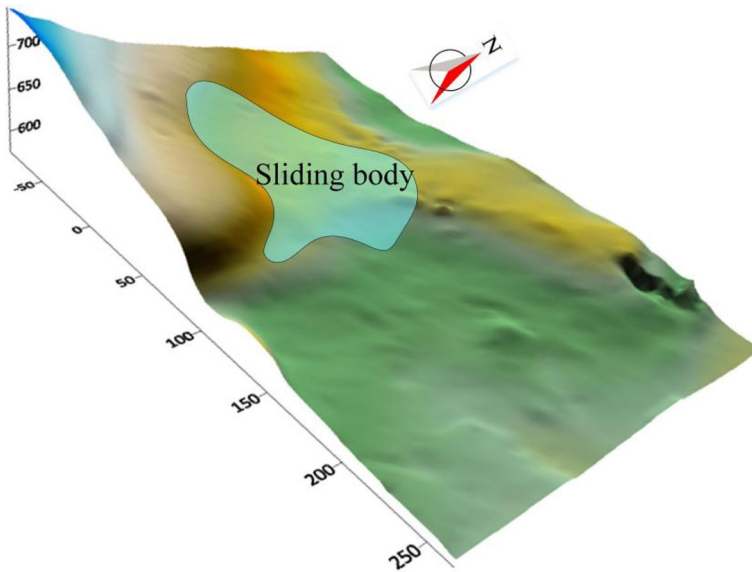


**Fig. 3** Elevation surfaces for Pangjiawan landslides

### 2.3 Failure mechanisms of landslide

The formation mechanism of landslides is mainly due to the combined effects of stratum geotechnical properties, surface water infiltration, and topography. The material composition of the soil in the landslide stratum is mainly earthy yellow clay with gravel, with the presence of voids. In the area where the landslide occurred, long-term atmospheric rainfall occurred with high amounts of water. A large amount of surface water penetrates downwards along the voids inside the soil and flows through the rock-soil interface, which softens the soil, increases the weight, and reduces the shear strength of the soil-rock contact zones. Over time, it will provide conditions for the formation of a landslide sliding surface.

From Figs. 3 and 4, the landslide area can be seen to belong to the mountain-notch topography, which provides spatial conditions for transporting and accumulating weathered rock spalling from the upper landslide. It is also conducive to the accumulation of surface water in the region. The landslide elevation difference is large, and the soil produces a large downward sliding component along the bedrock surface under gravity and spatial conditions for creeping deformation or even shearing out. A combination of internal geological conditions and external natural camping forces eventually lead to landslides.

## 3 Landslide model

In this paper, PFC3D is applied to simulate the motion process of the Pangjiawan landslide with a certain amount of particles and rigid walls. This method can simulate the discontinuity features and complex paths of the sliding body during the landslide movement (Shi et al. 2021; Wang et al. 2020; Zhuang et al. 2022).

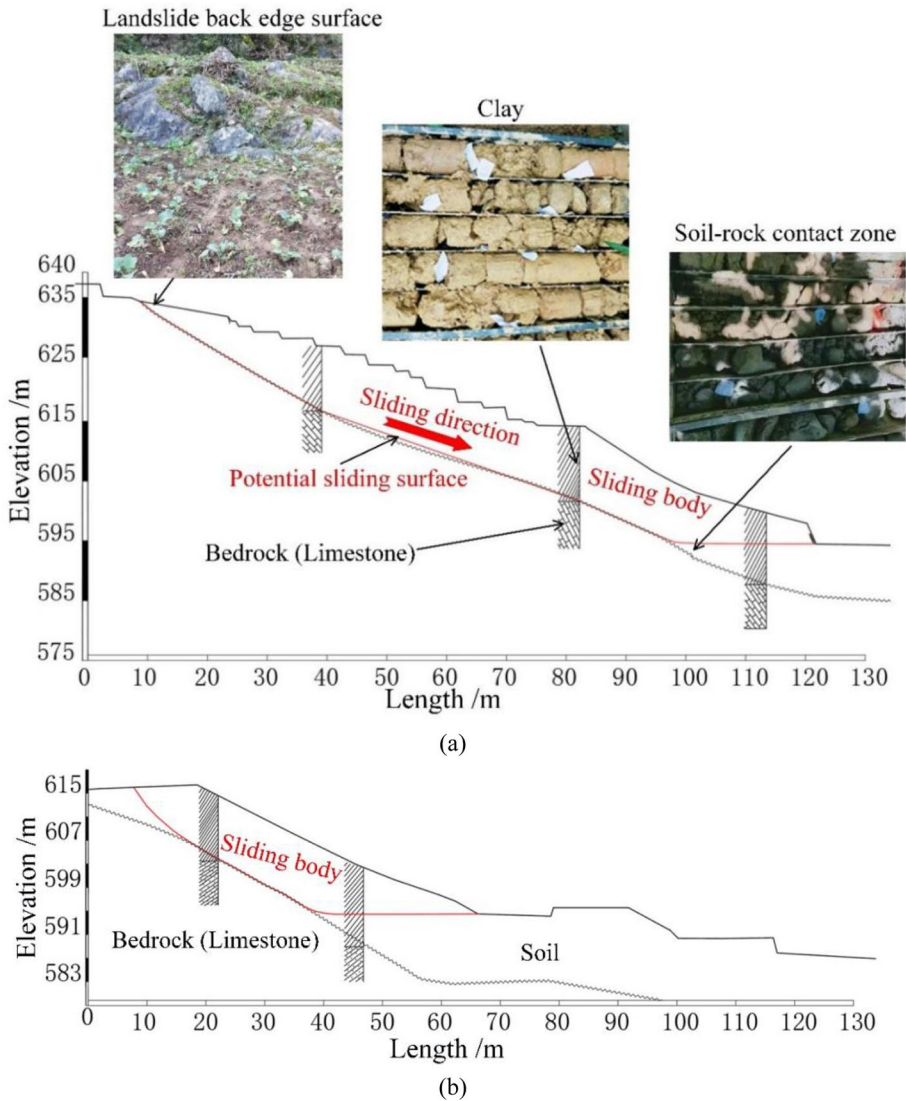
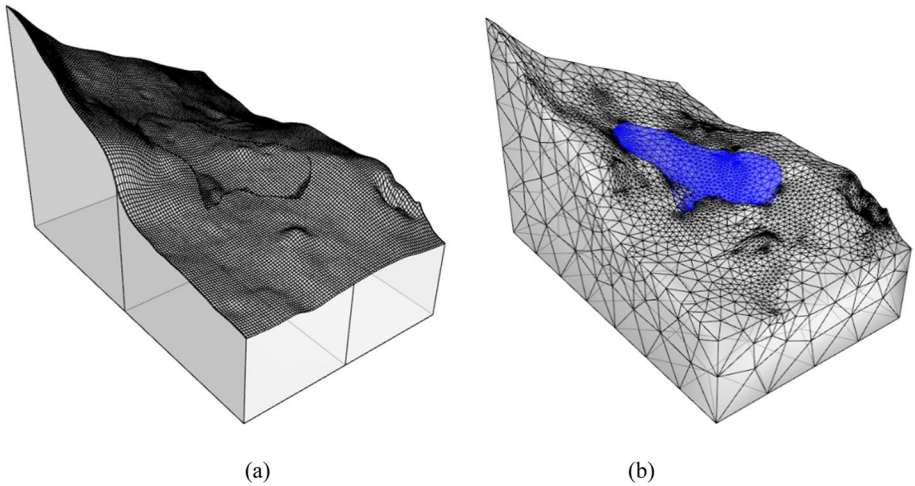


Fig. 4 Geological sections of the Pangjiawan landslide: a Section I-I; b Section II-II

### 3.1 Geological models

To study the influence of the topography of the landslide area on the landslide movement path, three-dimensional geological modeling in PFC3D was carried out from digital elevation data, the original surveys, and the drilling data of the Pangjiawan landslide. Figure 5 shows the 3D Geological model of the study area. The model of bedrock-sliding body area was created with cloth curtain surfaces from elevation data to make the mesh more uniform. The location of the landslide surface and the sliding body were determined by the difference method, as shown in the blue part of Fig. 5b. The bedrock mesh and the



**Fig. 5** 3D Geological model of the study area: **a** The mesh model of landslide area; **b** The model of sliding body area (blue part)

slip surface were imported into the PFC3D separately via Fish language and dxf format files. The sliding surface and body are modeled by wall elements and particle elements in PFC3D (Fig. 6).

The landslide model has dimensions of 330 m in length, 210 m in width, 152.2 m in maximum surface elevation difference, and 43 m in maximum elevation difference at the sliding body. It comprises 7297 wall elements for the sliding surface and 295,869 particle elements forming the sliding body. Field investigations revealed that the size of sliding body clay material with several millimeters. Considering computational efficiency, the particle size range was enlarged from 0.45 to 0.675 m, with a scaling ratio of roughly 250 times.

### 3.2 Calibration of micro-parameters

The micro-parameters of particles need to be designated to simulate the macroscopic properties of the rock-soil mass in a PFC model (Gu et al. 2020; Yin et al. 2020). The trial-and-error method is currently the most common means of calculating the relationship between

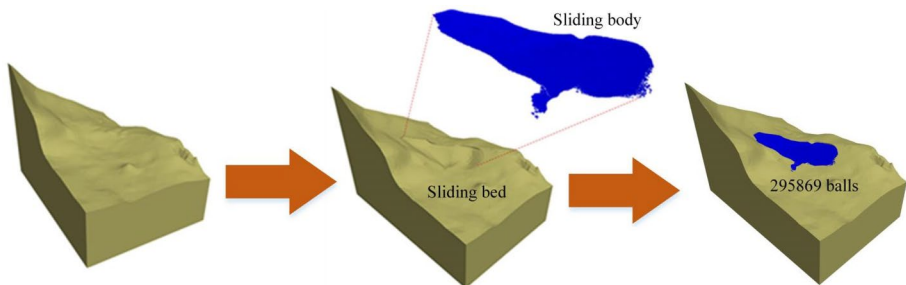


**Fig. 6** PFC3D modeling process of Pangjiawan landslide

micro- and macro-parameters (Lu et al. 2014; Potyondy and Cundall 2004). Based on the field geology investigation data, the density, void ratio, internal friction angle, and cohesion of the sliding clay macro-parameters is about  $1980 \text{ kg m}^{-3}$ , 0.7,  $14.6^\circ$ , and 27.4 kPa. A series of numerical direct shear tests were conducted with different shear stresses to calibrate the micro-parameters depending on the clay macro-parameters. The soil samples were created as follows:

- (1) Based on a magnification factor of 250 times the particle size, the box was scaled up to a diameter of 15.0 m and a height of 2.5 m by an equal scale factor. The “wing wall” was also created on both sides of the upper and lower shear box joints to prevent particles from flying out of the shear box during the shearing process, as shown in Fig. 7a. A total of 6745 particles with diameters of 0.450–0.675 m were generated in the box;
- (2) Gravity was applied to all particles and the initial balancing of the model was carried out according to the set contact model. For the contact of the sliding soil with powdered clay characteristics, the Adhesive Rolling Resistance Linear Model, based on the two-dimensional model of Gilabert et al. (2007, 2008), was used to simulate the cohesive characteristics. The Adhesive Rolling Resistance Linear Model provides the behavior of a cohesive granular material via a short-range attraction, as a linear approximation of the van der Waals interaction, by adding a cohesive component to the Rolling Resistance Linear Model (Inc., 2019);
- (3) The model was subjected to normal stress under four conditions: 50 kPa, 100 kPa, 150 kPa, and 200 kPa. A constant horizontal shear speed was applied to the bottom shear box by servo control, and the top shear box was kept still in the shearing process. When the shear displacement reached 2.0 m, the test was stopped.

In servo-controlled simulations, if the shear rate is set too fast, the specified stress state may be reached superficially, but the equilibrium stress level is actually lower than the measured level. So, to keep the system in static equilibrium, the inertia number can be used to determine that the simulation is in a quasi-static state (Cruz et al. 2005; O’Sullivan 2011; Radjai 2009), and the three-dimensional inertia number can be calculated by the following equation:

$$I = \dot{\epsilon}_q \sqrt{\frac{m}{pd}} \quad (1)$$

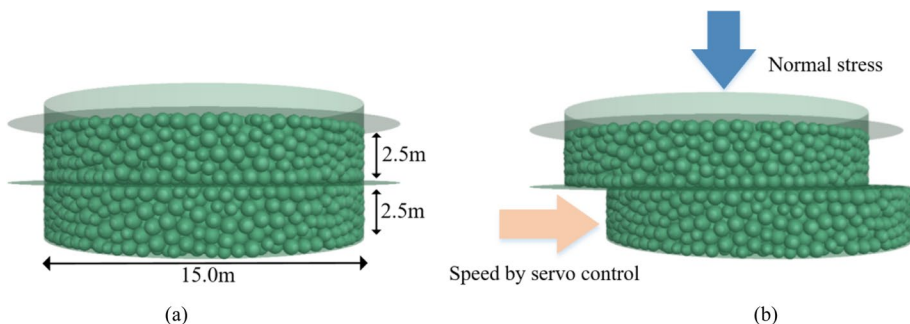


**Fig. 7** DEM modeling of direct shear tests: **a** Model before the test; **b** Model after the test



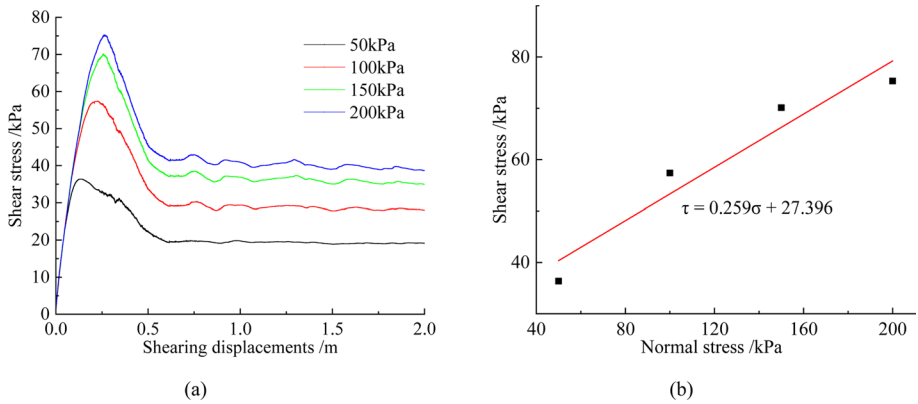


**Fig. 8** Calibration process of micro-parameters through direct shear tests: **a** Relation between shear stress and shearing displacement in DEM model; **b** Relation between shear stress and normal stress in DEM model

**Table 1** Micro-parameters of the model

Parameter	Value
Minimum radius/m	0.45
Rmax/Rmin	1.5
Particle density/kg·m <sup>-3</sup>	2500
Porosity	0.3
Particle effective modulus/MPa	55
Normal-to-shear stiffness ratio	1.0
Coefficient of friction	0.174
Attractive force/Pa	1000
Attraction range/m	0.026

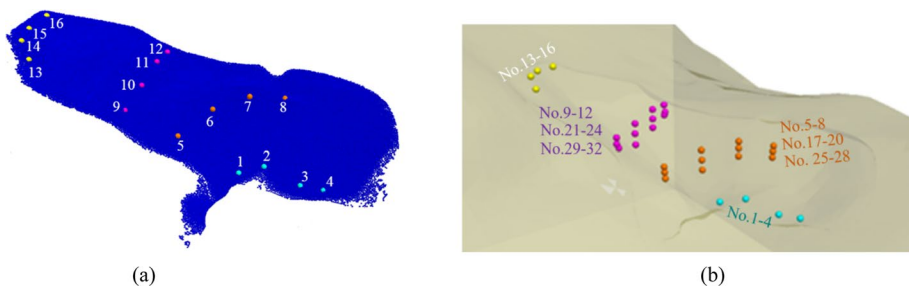
where  $\dot{\epsilon}_q$  is the shear strain rate,  $m$  is the particle mass,  $d$  is the particle diameter, and  $p$  is the surrounding pressure. After experimental comparison, the smaller the shear speed, the smaller the shear strength. Considering the calculation efficiency, the straight shear test rate was taken as 0.01 m/s.

After continuous adjustment of the micro-parameters and a large number of repeated numerical tests, the numerical test results of direct shear and indoor test results coincided, as shown in Fig. 8. Micro-parameters corresponding to the particles and Adhesive Rolling Resistance Linear Model were obtained (Table 1).

The generated particles were assigned the corresponding particle micro-parameters in Table 1. After the contact forces and contact moments on the particles were zeroed, the solution was executed by the convergence condition “model solve ratio-average 1e-4 cycle 10,000,” and this equilibrium state was the initial state of the landslide model. Subsequently, similar to the field, gravity was used as the source of the sliding force, to simulate the landslide’s motion process. The solution was executed by the convergence condition “model solve ratio-average 1e-5 cycle 20,000.” The final landslide simulation time was 504 s and it took about 8 days on a workstation (Intel I9-9900 K and 32 GB RAM).

**Table 2** Number of monitoring points

The front edge of the landslide	The middle of the landslide (in the front)			The middle of the landslide (in the back)			The back edge of the landslide
	Surface	Interior	Bottom	Surface	Interior	Bottom	
1	5	17	25	9	21	29	13
2	6	18	26	10	22	30	14
3	7	19	27	11	23	31	15
4	8	20	28	12	24	32	16

**Fig. 9** Location of monitoring points: **a** Surface distribution of monitoring points; **b** Distribution of each monitoring site

### 3.3 Monitoring points setting

In order to conduct a comprehensive analysis of the sliding characteristics of the Pangjiawan landslide on a spatial scale, the particles on the surface of the landslide, the interior of the landslide, the bottom of the landslide (at the front edge), the middle of the landslide (in the front), the middle of the landslide (in the back), and the back edge of the landslide were selected as monitoring points in this paper. The numbers of the monitoring points are shown in Table 2. A total of 32 locations were selected as monitoring points and Fig. 9 shows their location in the model.

## 4 Landslide mobility characteristics

### 4.1 Movement path

To analyze the movement path of the landslide, the particle displacement vector field was utilized to observe particle movements, visualizing the sliding direction, as shown in Fig. 10. The Pangjiawan landslide exhibits a complex movement path with turning and coalescence behavior throughout its progression. Initially, the soil in the mountain-notch topography slides and undergoes deflective motion (Fig. 10a). Subsequently, the soil at the rear of the northwestern and northeastern areas of the landslide initiates sliding (Fig. 10b), and the trend of the landslide movement becomes more apparent with time (Fig. 10c).

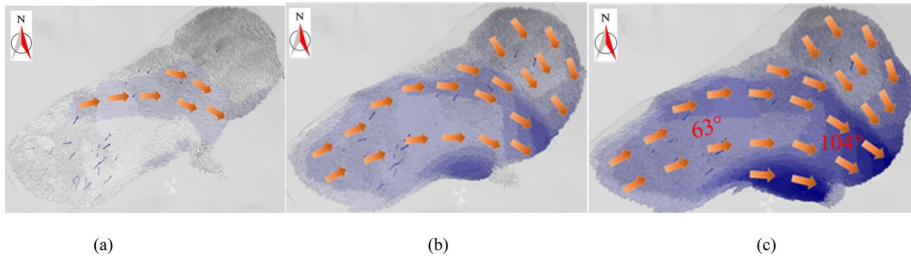


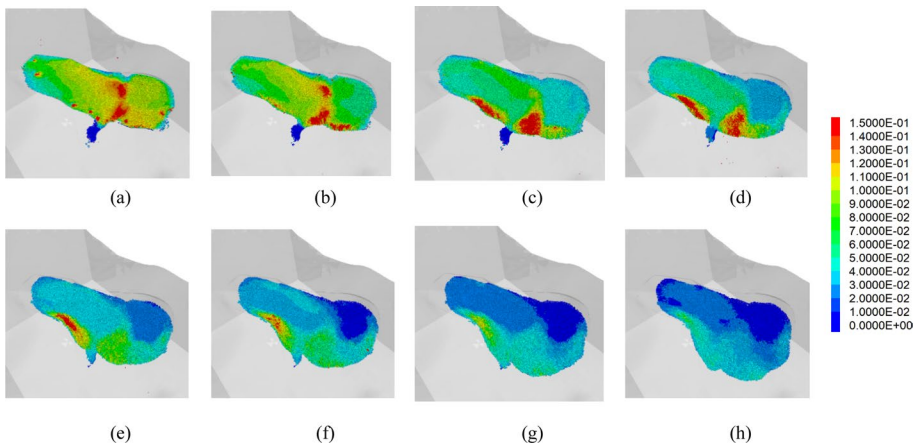
**Fig. 10** landslide movement direction at different times: **a** 54 s; **b** 204 s; **c** 504 s

Sliding bodies in the northeastern and northwestern areas eventually converge at the shear outlet at the front edge of the landslide. The direction of movement of the soil at the rear of the landslide is about  $63^\circ$ . The direction is deflected to  $104^\circ$  when the movement reaches the middle of the landslide, aligning with the landslide movement determined by on-site investigation (Fig. 2).

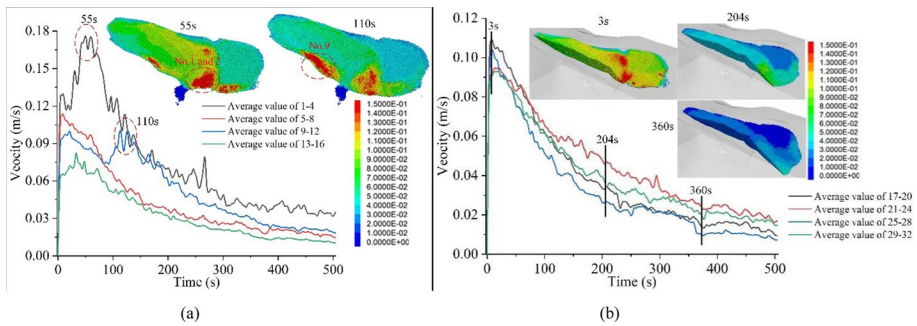
### 4.2 Velocity field

Figure 11 shows the velocity field at different times during the landslide motion. Within a brief duration (3 s), particle movement velocities at various locations of the landslide increased rapidly. The velocity at the front edge and middle of the landslide is particularly noteworthy (Fig. 11a). The overall landslide velocity continues to rise, with the majority of sliding bodies reaching velocities of 0.08 m/s. At 42 s, the sliding body progresses to the foot of the mountain (the front edge of the landslide) in a flat and open terrain (Fig. 11b). After 360 s, the particles move at a low velocity. The sliding body gradually comes to a halt and accumulates in the flatter terrain at the front edge of the landslide.

Average values of the monitoring points at different locations were calculated, as shown in Fig. 12. In Fig. 12a, at 3 s, when a landslide occurs, the velocity increases along the



**Fig. 11** Velocity field at different times: **a** 3 s; **b** 42 s; **c** 90 s; **d** 120 s; **e** 204 s; **f** 255 s; **g** 360 s; **h** 504 s (Unit: m/s)



**Fig. 12** Average velocity of monitoring point: **a** Surface of the landslide, No. 1–16; **b** Inside of the landslide, No. 17–32

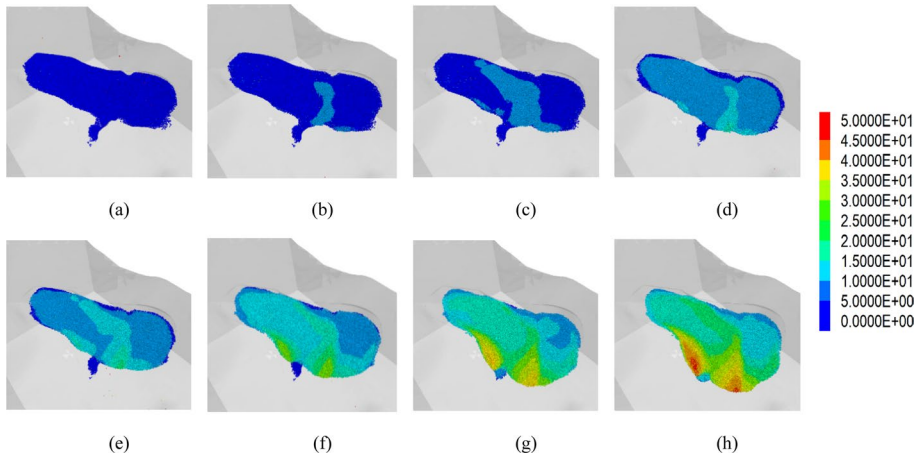
landslide direction, reaching the maximum velocity at the front edge of the landslide (Nos. 1–4) and the minimum velocity at the rear edge of the landslide (Nos. 13–16). During the sliding process, the velocity at the front edge of the landslide, especially at No. 1 and 2 (the cloud in Fig. 12a), continues to increase until 55 s. The velocity at the middle and rear of the landslide (Nos. 9–12) decreases, but it subsequently increases from 100 to 120 s, influenced by the movement of No. 9 in the undulating terrain (the upper-right cloud in Fig. 12a). Figure 12b shows the velocity inside the landslide. After 3 s, when a landslide occurs, the velocity of the landslide decreases over time. Compared with the velocity at the landslide’s surface, the velocity inside the landslide is smaller. As the depth of the sliding body increases, along with additional earth pressure and particle-to-particle constraints, the soil inside the landslide becomes more resistant to sliding than the soil on the landslide surface.

Based on the velocity field changes of the landslide, the movement phases of the landslide surface can be divided into initiation, acceleration, deceleration, reacceleration, and quiescence, influenced by topographic features and gravity. The movement phases of the sliding body inside the landslide can be divided into initiation, acceleration, deceleration, and quiescence, only affected by gravity.

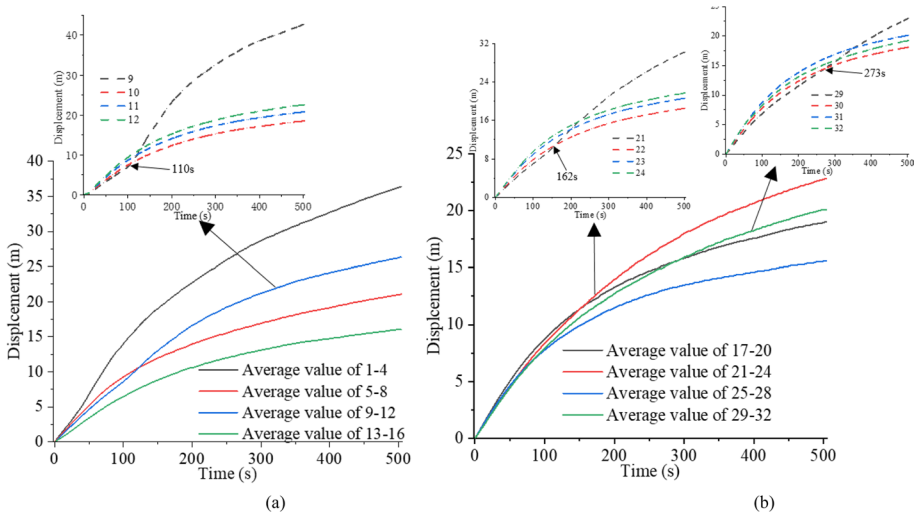
### 4.3 Displacement field

Figure 13 illustrates the displacement field at different times during the landslide motion. The soils at the front edge of the landslide start to displace (Fig. 13b), and the displacement distribution is deflected along the movement path (Fig. 13c). The deformation of the landslide extends rearward from the front edge, resulting in an overall increase in deformation (Fig. 13d). Following this, a substantial volume of soil slides out through the shear outlet and accumulates at the front edge of the landslide (Fig. 13e–h).

The average values of the monitoring points at different locations were calculated to observe the displacement changes, as shown in Fig. 14. The average maximum displacement reaches 36.4 m at the front edge of the landslide. The displacement on the sliding surface exceeds that within the slide. In general, displacement increases along the landslide direction. However, monitoring points No. 9, 21, and 29, situated to the side of the notch with a notable difference in drop (Fig. 9), experience significant increases in displacement at 110 s, 162 s, and 273 s, respectively.



**Fig. 13** Displacement field at different times: **a** 3 s; **b** 42 s; **c** 54 s; **d** 90 s; **e** 120 s; **f** 204 s; **g** 360; **h** 504 s (Unit: m)



**Fig. 14** Average displacement of monitoring point: **a** Surface of the landslide, No. 1–16; **b** Inside of the landslide, No. 17–32

As seen from the velocity and displacement fields of the landslide, the Pengjiawan landslide exhibits the deformation characteristics of a retrogressive landslide. The landslide initiates at the front edge and progresses to the rear edge, with the velocity and displacement evolving from the front to the back edge.

## 5 Scenario simulation of landslide model with arched anti-slide piles

### 5.1 Arched anti-slide pile layout

Based on the movement path of the sliding body and sliding force calculations, the arched anti-slide piles are arranged in the middle and front edge of the landslide, as shown in Fig. 15. From Fig. 15c, the middle and the front edge of the landslide both happened at the distinctive mountain-notch topography, and the bedrock on both sides of the sliding body has greater thickness and better structural stability compared to the bedrock in the lower part of the sliding body. Arched anti-slide piles were employed to better utilize bedrock on both sides of the slide. The middle of the landslide adopts the structural style of arched anti-slide piles + anti-slide retaining wall (Section I-I). The front edge of the landslide adopts the structural style of arched anti-slide piles (Section II-II) (Fig. 15c).

The simulation results and field investigation data reveal turning behavior in the middle edge and both turning and coalescence behaviors at the front edge of the Pangjiawan landslide (Fig. 10). To further analyze the effectiveness of arched anti-slide piles in the management of landslides with complex paths, the layout of arched anti-slide piles in the middle (Section I-I) is kept unchanged, and the layout of arched anti-slide piles in the front edge (Section II-II) with different rise-span ratios and pile spacings is discussed in depth. To mitigate the impact of topographic conditions on the embedded depth of the anti-slide pile, rise-span ratios of anti-slide piles (0.00, 0.06, 0.08, 0.09, and 0.10) were chosen, maintaining a pile spacing of 5.0 m. Similarly, keeping the rise-span ratio as 0.1, pile spacing

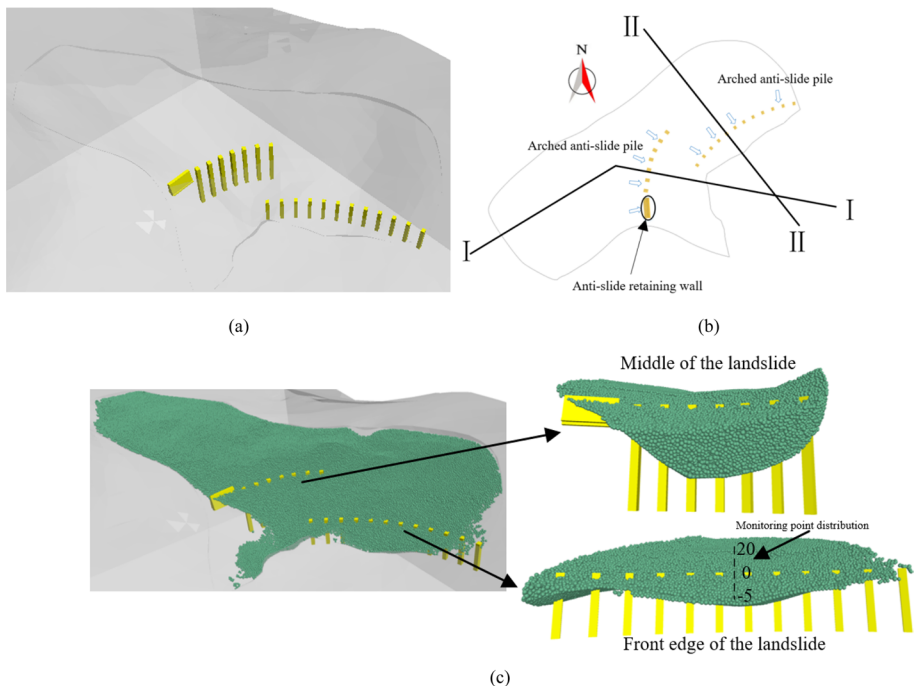


**Fig. 15** Landslide reinforced by the arched anti-slide piles with 5 m spacing and 0.1 rise-span ratios in the front edge of the landslide: **a** Layout without soils; **b** Layout; **c** Holistic model

(5.0 m, 5.5 m, 6.0 m, 7.5 m) was selected for analysis. In total, eight different working conditions were calculated, as shown in Table 3. The length of the free section is about 4.9 m and the embedded section of the arched anti-slide pile is about 5.1 m in each condition.

In the landslide model with arched anti-slide piles, the piles and retaining wall are treated as rigid materials, and deformation is neglected. Soil parameters remain constant, and the initial values of the particle's displacement and velocity fields are set to zero. Gravity serves as the driving force for sliding. The solution is implemented using the convergence condition "model solve ratio-average  $1e-5$  cycle 20,000" in the PFC software.

## 5.2 Displacement of sliding body analysis

### 5.2.1 Different rise-span ratios

Figure 16 shows landslide displacement under arched anti-slide piles with different rise-span ratios and a pile spacing of 5.0 m. It should be noted that, as shown in Fig. 16a, the distribution of anti-slide piles is locally adjusted by the influence of topography when the rise-span ratio is 0.0. On the left side of the landslide, the combined support of the arched anti-slide pile + anti-slide retaining wall (Section I-I) results in minimal overall displacement ( $<0.01$  m), and the combined support with the arched anti-slide pile significantly enhances landslide stability, particularly during turning behavior. On the right side and the front edge of the landslide, the larger the rise-span ratio of the arched anti-slide pile (Section II-II), the smaller the landslide displacement. With a rise-span ratio of  $f/l=0$ , the anti-slide pile distribution follows a conventional linear style, resulting in the most noticeable displacement in the right side area of the landslide (Fig. 17a). The center line of the arched anti-slide pile at the front edge of the landslide serves as the monitoring point (Fig. 15c). The displacement distribution under the anti-slide pile with different rise-span ratios is shown in Fig. 16. The rise-span ratio of the anti-slide pile varies from 0.00 to 0.06, resulting in an order of magnitude reduction in the displacement of the monitoring point. When the rise-span ratio is 0.1 ( $f/l=0.1$ ), the landslide exhibits no deformation. For landslide management characterized by turning and coalescence behavior, the arched anti-slide pile demonstrates superior support compared to the conventional linear anti-slide pile.

### 5.2.2 Different pile spacing

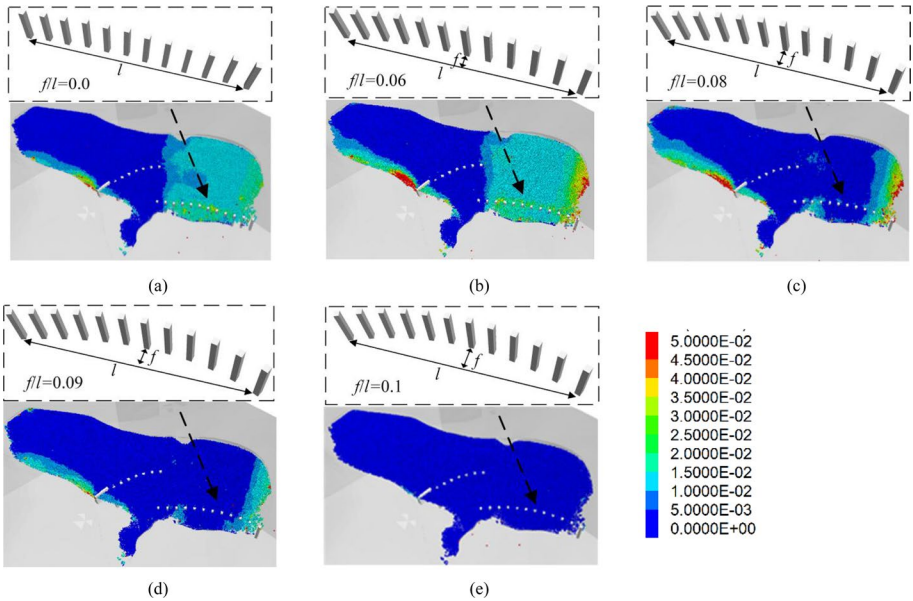
Figure 18 shows landslide displacement under arched anti-slide piles with different pile spacing and a rise-span ratio of 0.1. The longer the pile spacing, the more pronounced the landslide displacement. Importantly, the left side area of the landslide exhibits minimal displacement in various pile spacing, and the overall displacement also remains minor ( $<0.01$  m) after arched anti-slide piling reinforcement under different pile spacings. Figure 19 presents the displacement of the center line of arched anti-slide piles at the front edge of the landslide. The displacement of the centerline is most significant 5 m behind the piles, and it notably decreases beyond 10 m from the centerline of the pile. Within 10 m behind the arched anti-slide piles, uneven deformation of the landslide gives rise to a soil arch loading structure, ensuring landslide stability. This phenomenon becomes more noticeable with longer pile spacing. Increased pile spacing weakens the interaction between the piles and soil, facilitating the sliding of landslide soil between the piles.

**Table 3** Layout parameters of arched anti-slide piles

Section	Structural style	Cross-section size $S$	Height $H$	Spacing $\Delta L$	Rise-span ratio $f/l$
Section I-I	Anti-slide retaining wall	10.0 m $\times$ 1.2 m (wall); 10.0 m $\times$ 0.3 m (Wall toe step); 10.0 m $\times$ 1.0 m (Anti-slide tenon)	5.0 m (Face slope ratio 1:0.25); 0.5 m (Wall toe step); 0.5 m (Anti-slide tenon)	–	–
Section II-II	Arched anti-slide piles	1.5 m $\times$ 2.0 m	19 m	5.0 m (7 piles in total)	0.12
	Arched anti-slide piles	1.25 m $\times$ 1.50 m	10 m	5.0 m (12 piles in total)	0.10
				5.5 m (11 piles in total)	
				6.0 m (10 piles in total)	
				7.5 m (8 piles in total)	
				5.0 m (12 piles in total)	0.09
					0.08
					0.06
					0.00

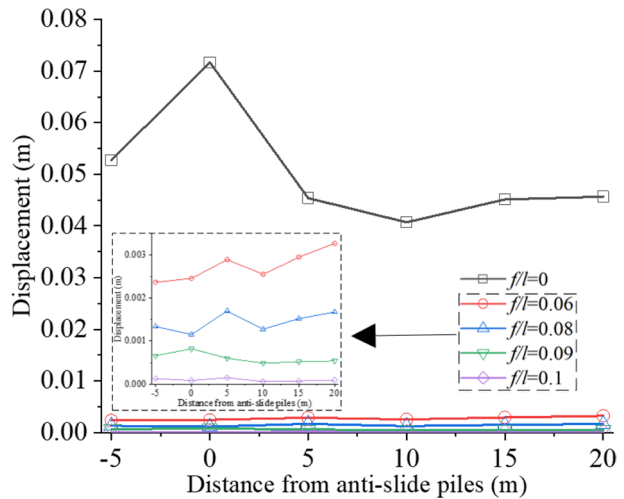
$f$  is the height of the arch and  $l$  is the span of the arch





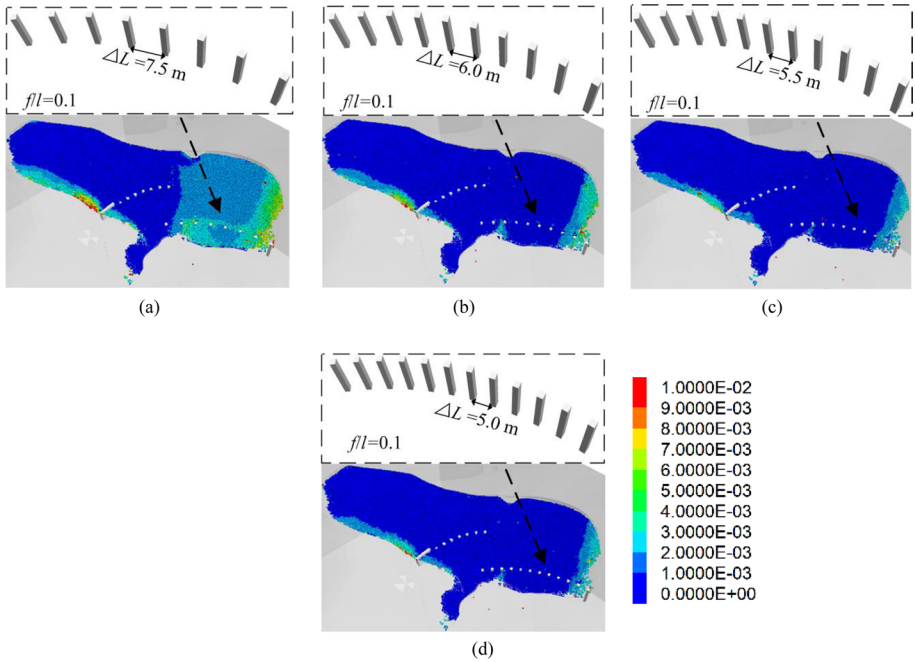
**Fig. 16** Landslide displacement field with different rise-span ratios: **a**  $f/l=0.0$ ; **b**  $f/l=0.06$ ; **c**  $f/l=0.08$ ; **d**  $f/l=0.09$ ; **e**  $f/l=0.1$  (Unit: m)

**Fig. 17** Landslide displacement at the center line of the anti-slide pile with different rise-span ratios



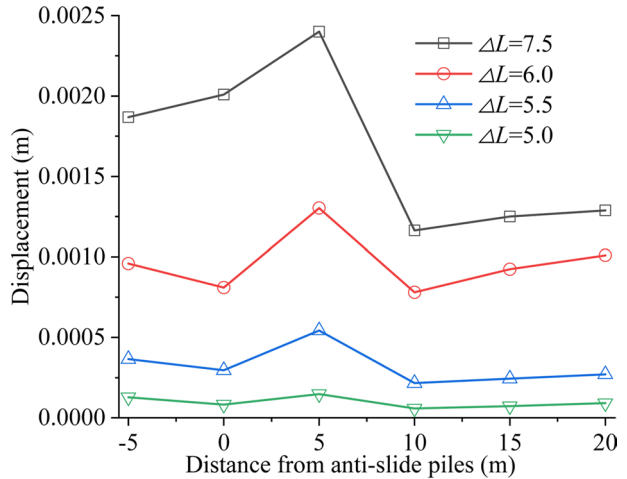
### 5.3 The contact force of piles analysis

Figure 20 shows the contact force distribution cloud of the arched anti-slide pile on the front edge and the middle of the landslide after stabilization. Due to the influence of the notch topography, the maximum value of contact forces is located at the top of the arch structure (the middle of the arched anti-slip piles) in both Section I-I and Section II-II. It is worth noting that in different working conditions, the contact force of the arched



**Fig. 18** Landslide displacement field with different spacing: **a**  $\Delta L=7.5$  m; **b**  $\Delta L=6.0$  m; **c**  $\Delta L=5.5$  m; **d**  $\Delta L=5.0$  m (Unit: m)

**Fig. 19** Landslide displacement at the center line of the arched anti-slide pile at the front edge of the landslide



anti-slide piles in the middle of the landslide (Section I-I) is roughly similar (Fig. 20b), and because of the more pronounced topography of the notch in the middle of the landslide compared to that at the front edge, the maximum contact forces in the middle are more significant,  $7.68e6$  N.

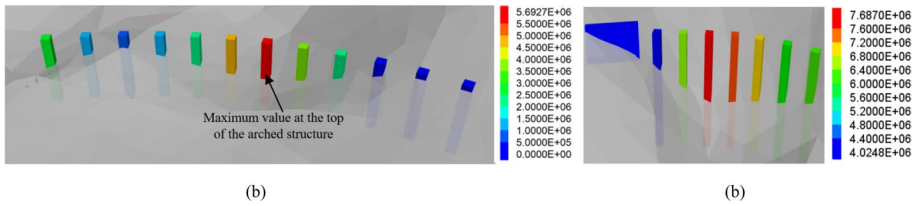


**Fig. 20** Contact force distribution of the arched anti-slide pile with 5 m spacing and 0.1 rise-span ratios in the front edge of the landslide and the arched anti-slide pile with 5 m spacing and 0.12 rise-span ratio in the middle of the landslide (Section II-II): **a** the front edge of the landslide; **b** the middle of the landslide (Section I-I)

Figure 21 shows the contact force distribution of the arched anti-slide pile at the front edge of the landslide. In Fig. 21a, when the rise-span ratios of the arched anti-slide piles increase from 0.06 to 0.10, the contact force remains relatively stable, except at the top of the arch structure (the middle of the arched anti-slide piles). The contact force of conventional linear anti-slide piles ( $f/l=0$ ) is minimal, however, corresponding to the largest landslide displacement (Fig. 16a). This suggests that the structure ( $f/l=0$ ) does not fully utilize the synergistic effect between pile and soil. Considering the analysis in Figs. 16 and 17, the larger the arched anti-slide pile rise-span ratio is, the smaller the landslide displacement is. This implies that the increase in the rise-span ratios has minimal impact on the pile forces but enhances the synergy between piles and soil, contributing to the stability of the sliding body.

Figure 21b indicates that a larger pile spacing corresponds to a greater contact force of the arched anti-slide pile, especially between  $-15$  m and  $0$  m from the middle of the arched anti-slide piles. The pile spacing's increase results in higher pressure on the piles at the top of the arch structure. The effectiveness of the piles on both sides of the arch structure weakens in sharing the load of the piles in the middle. This observation suggests that an increase in the pile spacing of the arched anti-slide piles leads to an elevated strength requirement for the central anti-slide pile.

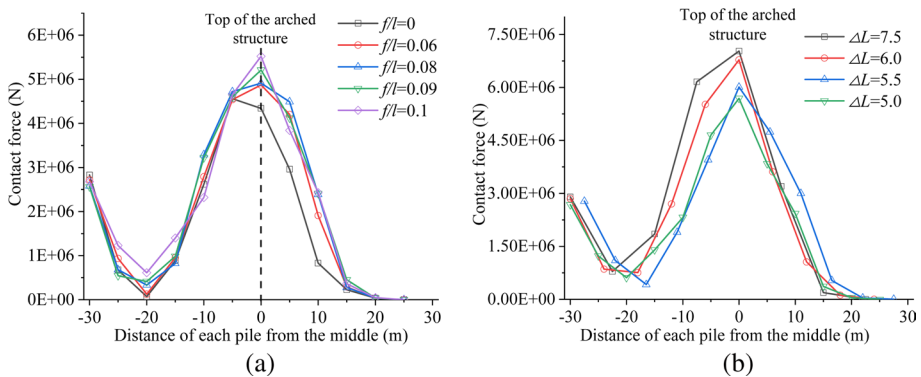


**Fig. 21** Contact force distribution of the arch anti-slide pile at the front edge of landslide: **a** the arched anti-slide piles with a spacing of 5.0 m and different rise-span ratios; **b** the arched anti-slide piles with rise-span ratios of 0.1 and different pile spacing

Furthermore, the uneven distribution of landslide force among the piles is attributed to the topography of the notch. In each different working condition, the contact force of the anti-slide pile at the bottom of the arch structure ( $\pm 20$  m from the middle of the arched anti-slide pile) is about 88.48% smaller than that of the anti-slide pile at the top of the arched structure (the middle of the arched anti-slide pile). Arched anti-slide piles at different locations should not adhere to a uniform reinforcement design during field construction. The adoption of the maximum internal force to standardize the reinforcement of each pile would inevitably result in significant wastage.

## 6 Discussion

The complexity of landslide movement paths introduces the uncertainty of landslide movement paths, challenging landslide hazard prediction and pre-disaster prevention and control (Shi et al. 2021; Zhou et al. 2015). Numerical simulation of geohazard chains is considered the most effective method to reveal the dynamics process with complex paths of landslides and the scenario analysis of potential landslides (Wang et al. 2020). In contrast to traditional numerical simulation methods for continuous media used to study the initiation mechanism and characteristics of post-landslides, the DEM has obvious advantages in simulating the discontinuous deformation and landslide movement paths with different scenario analyses (Zhuang et al. 2022). The PFC method, one of the widely used DEM methods, elucidates runout mechanisms at different depths of the sliding body by tracking the velocity, displacement, and hazard chain during Pangjiayan landslide simulation (Figs. 12 and 14). The Adhesive Rolling Resistance Linear Model is employed to simulate the clay granular material of the sliding body, reflecting visco-frictional behavior rather than brittle failure behavior between materials, ensuring technical soundness (Figs. 7 and 8). In comparison with field observations, the Pangjiawan landslide movement path with turning and coalescence behavior, influenced by topographic changes, generally aligns with the actual situation (Figs. 2 and 10).

Cantilever and anchor cable anti-slide piles are widely used engineering measures when dealing with landslide hazards in mountainous-notch topography. However, when dealing with central sliding bodies that are thicker than the sides (Fig. 15) in distinctly notch topography, conventional designs need to consider longer free sections, wider cross sections, or the use of double rows of cantilevered anti-slip piles to control the central sliding body, which inevitably increases the project cost. For anchor cable anti-slide piles, although anchor cables can enhance the force state of the piles, anchor cables' presence significantly increases the construction cost and also poses technical challenges, especially in mountainous areas that are susceptible to rainfall and may face problems such as corrosion (Xu 2012). For landslides occurring in distinctly notch topography, arch anti-slide pile reinforcement structures have been proposed (Zhang and Deng 2013). It directly utilizes stable geotechnical bodies as the arch foot on both sides, reducing force requirements for each pile. The arch structure's bearing system, with small bending moments and large axial forces, maximizes the compressive performance of the concrete structure (Pan et al. 2001). In reinforcing the Pangjiawan landslide with mountain-notch topography exhibiting turning and coalescence, arched anti-slide piles maintain an advantage over traditional linear anti-slide piles ( $f/l=0$ ) (Fig. 15). With the rise-span ratio of the anti-slide pile changing from 0.0 to 0.06, the monitoring point displacement reduces significantly.

To minimize construction costs and optimize the collaboration between piles and soil, it is necessary to design and construct anti-slide pile structures by considering the engineering geological characteristics of specific landslides. Maintaining a consistent embedded depth, the rise-span ratio of the arched anti-slide pile changes from 0.06 to 0.1. The larger the rise-span ratio of the arched anti-slide piles, the smaller the landslide displacement (Fig. 14). However, the impact on pile forces from increasing rise-span ratios is minimal, except for the force at the top of the arch structure system (Fig. 19a). It means that higher rise-span ratios enhance the synergy between piles and soil, contributing to greater stability in the sliding body. Excessive rise-span ratios, elevating the force at the top of the arch structure system, may render the arched anti-slide piles unstable. Maintaining a rise-span ratio of 0.1, the larger the pile spacing of the arched anti-slide pile, the greater the landslide displacement, and the greater the contact force of the arched anti-slide pile (Fig. 16 and 17). Nevertheless, even with increased spacing and reduced anti-slide pile quantity, the landslide displacement post-reinforcement with arched anti-slide piles remains smaller than that with traditional linear anti-slide piles, signifying an effective support mechanism. Therefore, with robust piles and utilizing the arch structure system, a reasonable reduction in the number of arched anti-slide piles can be implemented, enhancing the cost-effectiveness of the landslide support design scheme.

In notch mountainous topography, employing arched anti-slide piles is beneficial when facing significant landslide thrust. In such cases, the arch structure can incorporate a link beam with a specified stiffness between the piles. This addition aids in efficiently transferring the load along the primary slide direction of the landslide to either the anti-slide piles on both sides of the landslide or the rock layer with more favorable geological conditions.

## 7 Conclusions

In this study, a comprehensive investigation encompassing field assessments, dynamic analysis of the Pangjiawan landslide, and engineering-scale discrete element simulations was undertaken to unravel the intricate motion characteristics of the landslide phenomenon. Furthermore, considering varying pile spacing and rise-span ratios, we meticulously evaluated the effectiveness of reinforcing the landslide with arched anti-slide piles. The primary conclusions derived from this work are as follows:

1. The complex movement path of the Pangjiawan landslide, influenced by the rugged mountain-notch topography, is characterized by distinctive turning and convergence behaviors during its progression. Remarkably, the direction of movement shifts from an angle of  $63^\circ$  to  $104^\circ$ , with distinct sliding bodies from the northeast and northwest regions converging at the shear outlet of the landslide.
2. The Pangjiawan landslide exhibits a retrogressive damage mode, where velocity and displacement patterns evolve from the front edge towards the rear. Notably, the most prominent velocity changes occur at the front edge and mid-section of the landslide. From the Pangjiawan landslide movement path of the numerical results, which generally aligns with the actual situation, it is demonstrated that the discrete element method is an effective tool for studying the process with complex paths of sliding.
3. For landslides within intricate notch topographies involving complex movement paths, such as turning and coalescence behaviors, arched anti-slide piles exhibit superior control efficacy compared to conventional linear anti-slide piles ( $f/l = 0$ ). When maintaining

a consistent embedded depth, higher rise-span ratios of arched anti-slide piles correspond to more pronounced synergistic effects between the piles and the surrounding soil, leading to reduced landslide displacement. Greater pile spacing of the arched anti-slide piles is associated with augmented landslide displacement and increased contact forces within the anti-slide pile system. Due to the uneven topography of the notch, the distribution of landslide forces among the piles is heterogeneous. Consequently, during practical implementation, the design of arched anti-slide piles at different locations should be tailored according to a non-uniform reinforcement approach.

In summation, this research advances our understanding of landslide dynamics with complex paths, particularly within the context of intricate mountain-notch topography. The research results provide a valuable reference for the reinforcement strategy of arched anti-slide piles in landslide treatment, especially when facing challenges brought by complex topographical environments.

**Acknowledgements** We appreciate the detailed suggestions and constructive comments from the editor and the anonymous reviewers.

**Author contributions** All authors contributed to the study's conception and design. Field investigation, data collection, and analysis were performed by HP and XF. Establishment of discrete element model was performed by ZC, RT and WC. The first draft of the manuscript was written by QX and ZC, and all authors commented on previous versions of the manuscript. All authors read and approved the final manuscript.

**Funding** This work was financially supported by Chongqing Education Commission of China (No. KJQN202004306), the graduate research and innovation foundation of Chongqing, China (Grant No. CYS23117), the Natural Science Foundation of Chongqing (CSTB2022NSCQ-MSX1466), Chongqing Planning and Natural Resources Bureau China (KJ-2023018 and No.DK2021Z05null01C), Chongqing Geological Disaster Prevention and Control Center (No. KJ2021050).

**Data availability** The data used to support the findings of this study are available from the corresponding author upon request.

## Declarations

**Conflict of interest** The authors have no relevant financial or non-financial interests to disclose.

## References

- Bessette-Kirton EK, Coe JA, Schulz WH, Cerovski-Darriau C, Einbund MM (2020) Mobility characteristics of debris slides and flows triggered by Hurricane Maria in Puerto Rico. *Landslides* 17(12):2795–2809
- Chen KT, Wu JH (2018) Simulating the failure process of the Xinmo landslide using discontinuous deformation analysis. *Eng Geol* 239:269–281
- Cruz FD, Emam S, Prochnow M, Roux JN, Chevoir F (2005) Rheophysics of dense granular materials: discrete simulation of plane shear flows. *Phys Rev E Stat Nonlinear Soft Matter Phys* 72:021309
- Cundall P, Strack O (1979) A discrete numerical model for granular assemblies. *Geotechnique* 29:47–65
- Evans SG, Hungr O, Clague JJ (2001) Dynamics of the 1984 rock avalanche and associated distal debris flow on Mount Cayley, British Columbia, Canada; implications for landslide hazard assessment on dissected volcanoes. *Eng Geol* 61:29–51
- Fan X, Dufresne A, Whiteley J, Yunus AP, Subramanian SS, Okeke CAU, Pánek T, Hermanns RL, Ming P, Strom A, Havenith HB, Dunning S, Wang G, Tacconi Stefanelli C (2021) Recent technological and methodological advances for the investigation of landslide dams. *Earth Sci Rev* 218:103646
- Froude MJ, Petley D (2018) Global fatal landslide occurrence from 2004 to 2016. *Nat Hazards Earth Syst Sci* 18:2161–2181

- Gao Y, Yin Y, Li B, Feng Z, Wang W, Zhang N, Xing A (2017) Characteristics and numerical runout modeling of the heavy rainfall-induced catastrophic landslide–debris flow at Sanxicun, Duijiangyan, China, following the Wenchuan Ms 8.0 earthquake. *Landslides* 14(4):1361–1374
- Gianvito S, Xuanmei F, Qiang X, Chun L, Chaojun O, Guillem D, Fan Y, Lanxin D (2018) Some considerations on the use of numerical methods to simulate past landslides and possible new failures: the case of the recent Xinmo landslide (Sichuan, China). *Landslides* 15(7):1359–1375
- Gilbert FA, Roux JN, Castellanos A (2007) Computer simulation of model cohesive powders: influence of assembling procedure and contact laws on low consolidation states. *Phys Rev* 75(1):011303
- Gilbert FA, Roux JN, Castellanos A (2008) Computer simulation of model cohesive powders: plastic consolidation, structural changes, and elasticity under isotropic loads. *Phys Rev* 78(3):031305
- Gu DM, Liu HL, Huang D, Zhang WG, Gao XC (2020) Development of a modeling method and parametric study of seepage-induced erosion in clayey gravel. *Int J Geomech* 20(12):04020219
- Hu XD, Zhang L, Hu KH, Cui L, Wang L, Xia ZY, Huang QZ (2022) Modelling the evolution of propagation and runout from a gravel–silty clay landslide to a debris flow in Shaziba, southwestern Hubei Province. *China Landslides* 19(9):2199–2212
- Hu XL, Tan FL, Tang HM, Zhang GC, Su AJ, Xu C, Zhang YM, Xiong CR (2017) In-situ monitoring platform and preliminary analysis of monitoring data of Majiagou landslide with stabilizing piles. *Eng Geol* 228:323–336
- Huang D, Li YQ, Song YX, Xu Q, Pei XJ (2019) Insights into the catastrophic Xinmo rock avalanche in Maoxian county, China: combined effects of historical earthquakes and landslide amplification. *Eng Geol* 258:105158
- Kim C, Kwon J, Im JC, Hwang S (2012) A method for analyzing the self-supported earth-retaining structure using stabilizing piles. *Mar Georesour Geotechnol* 30:313–332
- Kumar VS, Chandrasekaran SS (2022) Analysis of failure of high slope subjected to rainfall infiltration at Peringavu in Kerala, India *Eng Fail Anal* 138:106423
- Li LP, Lan HX (2021) Complexities of landslide moving path: a review and perspective. *Earth Sci* 47(12):4663–4680 (in Chinese)
- Li L, Lan H, Strom A (2020) Automatic generation of landslide profile for complementing landslide inventory. *Geomat Nat Haz Risk* 11:1000–1030
- Li B, Gong W, Tang H, Zou Z, Bowa VM, Juang CH (2021) Probabilistic analysis of a discrete element modelling of the runout behavior of the Jiweishan landslide. *Int J Numer Anal Method Geomech* 45(8):1120–1138
- Li XS, Fan W, Cao YB, Quan ZL (2022) MatDEM-based numerical simulation analysis of yanjiagou landslide evolution process. *Geol Resour* 30(2):199–206 (in Chinese)
- Lin CH, Lin ML (2015) Evolution of the large landslide induced by Typhoon Morakot: a case study in the Butangbunasi River, southern Taiwan using the discrete element method. *Eng Geol* 197:172–187
- Lo CM, Lin ML, Tang CL, Hu JC (2011) A kinematic model of the HsiaoLin landslide calibrated to the morphology of the landslide deposit. *Eng Geol* 123:22–39
- Lu CY, Tang CL, Chan YC, Hu JC, Chi CC (2014) Forecasting landslide hazard by the 3D discrete element method: a case study of the unstable slope in the Lushan hot spring district, central Taiwan. *Eng Geol* 183:14–30
- Meng HY, Zhan JW, Lu QZ, Yu ZY, Kang JL, Sun YM (2022) Kinematics characteristics and numerical simulation analysis of “8.12” giant landslide in Shanyang county, Shaanxi province. *J Eng Geol*. <https://doi.org/10.13544/j.cnki.jeg.2021-0645>. (in Chinese)
- O’Sullivan C (2011) Particulate discrete element modelling: a geomechanics perspective. Spon Press, Oxon
- Pan H, Yang XS, Wu SM (2001) Calculation of internal force and deformation of arch retaining structure. *J Build Struct* 22(5):93–96 (in Chinese)
- Potyondy D, Cundall P (2004) A bonded-particle model for rock. *Int J Rock Mech Min Sci* 41:1329–1364
- Radjai F (2009) Force and fabric states in granular media. Aip Conference
- Ray A, Verma H, Bharati AK, Rai R, Koner R, Singh TN (2022) Numerical modelling of rheological properties of landslide debris. *Nat Hazards* 110(3):2303–2327
- Schaefer LN, Santi PM, Duron TC (2021) Debris flow behavior during the September 2013 rainstorm event in the Colorado Front Range, USA. *Landslides* 18(5):1585–1595
- Shi C, De LI, Chen KH, Zhou JW (2016) Failure mechanism and stability analysis of the Zhenggang landslide in Yunnan Province of China using 3D particle flow code simulation. *J Mt Sci* 13(5):891–905
- Shi C, Li W, Meng Q (2021) A dynamic strain-rate-dependent contact model and its application in hongshiyang landslide. *Geofluids* 2021:9993693


- Tian XX, Song ZP, Zhang YW (2021) Monitoring and reinforcement of landslide induced by tunnel excavation: a case study from Xiamaixi tunnel. *Tunn Undergr Space Technol* 110:103796
- Usluogullari OF, Temugan A, Duman ES (2016) Comparison of slope stabilization methods by three-dimensional finite element analysis. *Nat Hazards* 81(2):1027–1050
- Wang HL, Liu SQ, Xu WY, Yan L, Xie WC (2020) Numerical investigation on the sliding process and deposit feature of an earthquake-induced landslide: a case study. *Landslides* 17(11):2671–2682
- Wei JB, Zhao Z, Xu C, Wen Q (2019) Numerical investigation of landslide kinetics for the recent Mabian landslide (Sichuan, China). *Landslides* 16(11):2287–2298
- Wu LL, He KQ, Guo L, Zhang J, Sun LN, Jia YY (2022) Research on the excavation stability evaluation method of Chaqishan ancient landslide in China. *Eng Fail Anal* 141:106664
- Wu JH, Lin WK, Hu HT (2017) Assessing the impacts of a large slope failure using 3DEC: the Chiu-fen-erh-shan residual slope. *Comput Geotech* 88:32–45
- Wu JH, Lin WK, Hu HT (2018) Post-failure simulations of a large slope failure using 3DEC: the Hsien-du-shan slope. *Eng Geol* 242:92–107
- Xie Q, Cao ZL, Shi XK, Fu X, Ban YX, Wu ZH (2021a) Model test of interaction between load-caused landslide and double-row anti-slide piles by transparent soil material. *Arab J Sci Eng* 46:4841–4856
- Xie Q, Cao ZL, Xie WB, Song ZP, Wu ZH (2021b) Model test and numerical analysis of cutting slope with skip cut method. *Nat Hazard Rev* 22(2):04021002
- Xu JZ (2012) Research on new anti-slip structures and their engineering applications. Xinan Jiaotong University, Chengdu, China (**in Chinese**)
- Xu LF, Meng XW, Xu XG (2014) Natural hazard chain research in China: a review. *Nat Hazards* 70(2):1631–1659
- Yin Y, Xing A, Wang G, Feng Z, Jiang Y (2016) Experimental and numerical investigations of a catastrophic long-runout landslide in Zhenxiang, Yunnan, southwestern China. *Landslides* 14(2):649–659
- Yin ZY, Wang P, Zhang F (2020) Effect of particle shape on the progressive failure of shield tunnel face in granular soils by coupled FDM-DEM method. *Tunn Undergr Space Technol* 100:103394
- Zhang HX, Lu KP, Zhang WZ, Li DL, Yang GL (2022a) Quantification and acoustic emission characteristics of sandstone damage evolution under dry-wet cycles. *J Build Eng* 48:103996
- Zhang JA, Kuang MX, Zhang YH, Feng TG (2022b) Evaluation and analysis of the causes of a landslide and treatment measures during the excavation of a tunnel through a soil-rock interface. *Eng Fail Anal* 130:105784
- Zhang S, Li C, Qi H, Chen X, Ma S (2021) Soil arch evolution characteristics and parametric analysis of slope anchored anti-slide pile. *KSCE J Civ Eng* 25:4121–4132
- Zhang ZW, Deng RG (2013) Theoretical study of spatial anti-slide structure of arc interval row piles with coupling beam on pile top. *Rock Soil Mech* 34(12):3403–3409 (**in Chinese**)
- Zhao B, Wang YS, Wang Y, Shen T, Zhai YC (2017) Retaining mechanism and structural characteristics of h type anti-slide pile (hTP pile) and experience with its engineering application. *Eng Geol* 222:29–37
- Zhou JW, Huang KX, Shi C, Hao MH, Guo CX (2015) Discrete element modeling of the mass movement and loose material supplying the gully process of a debris avalanche in the Bayi Gully, Southwest China. *J Asian Earth Sci* 99:95–111
- Zhu BB, Lei MF, Gong CJ, Zhao CY, Zhang YL, Huang J, Jia CJ, Shi CH (2022) Tunnelling-induced landslides: triggering mechanism, field observations and mitigation measures. *Eng Fail Anal* 138:106387
- Zhuang JQ, Jia KC, Zhan JW, Zhu Y, Zhang CL, Kong JX, Du CH, Wang SB, Cao YB, Peng JB (2022) Scenario simulation of the geohazard dynamic process of large-scale landslides: a case study of the Xiaomojiu landslide along the Jinsha River. *Nat Hazards* 112(2):1337–1357

**Publisher's Note** Springer Nature remains neutral with regard to jurisdictional claims in published maps and institutional affiliations.

Springer Nature or its licensor (e.g. a society or other partner) holds exclusive rights to this article under a publishing agreement with the author(s) or other rightsholder(s); author self-archiving of the accepted manuscript version of this article is solely governed by the terms of such publishing agreement and applicable law.



## Authors and Affiliations

Qiang Xie<sup>1</sup> · Zhilin Cao<sup>1</sup>  · Renjun Tian<sup>1,2</sup> · Weichen Sun<sup>1</sup> · Alessio Fumagalli<sup>3</sup> · Haiyou Peng<sup>1,4,5</sup> · Xiang Fu<sup>6</sup> · Haoyang Luo<sup>1</sup>

✉ Zhilin Cao  
icooolyes@qq.com

<sup>1</sup> School of Civil Engineering, Chongqing University, Chongqing 400045, People's Republic of China

<sup>2</sup> Guangzhou Urban Planning and Design Survey Research Institute, Guangzhou, People's Republic of China

<sup>3</sup> MOX Laboratory, Department of Mathematics, Politecnico di Milano, Via Bonardi 9, 20133 Milan, Italy

<sup>4</sup> Technology Innovation Center of Geohazards Automatic Monitoring, Ministry of Natural Resources, Chongqing, People's Republic of China

<sup>5</sup> Chongqing Institute of Geology and Mineral Resources, Chongqing, People's Republic of China

<sup>6</sup> College of River and Ocean Engineering, Chongqing Jiaotong University, Chongqing, People's Republic of China